

Simulations of hybrid charge-sensing single-electron-transistors and CMOS circuits

Tetsufumi Tanamoto¹ and Keiji Ono²

¹*Department of Information and Electronic Engineering,
Teikyo University, Toyosatodai, Utsunomiya 320-8551, Japan**

²*Advanced device laboratory, RIKEN, Wako-shi, Saitama 351-0198, Japan*

Single-electron transistors (SETs) have been extensively used as charge sensors in many areas such as quantum computations. In general, the signals of SETs are smaller than those of complementary metal-oxide semiconductor (CMOS) devices, and many amplifying circuits are required to enlarge these signals. Instead of amplifying a single small output, we theoretically consider the amplification of pairs of SETs, such that one of the SETs is used as a reference. We simulate the two-stage amplification process of SETs and CMOS devices using a conventional SPICE (Simulation Program with Integrated Circuit Emphasis) circuit simulator. Implementing the pairs of SETs into CMOS circuits makes the integration of SETs more feasible because of direct signal transfer from the SET to the CMOS circuits.

Single-electron transistors (SETs) have been intensively investigated owing to their advantages of low-power operation, which is desirable for application to logic and memory elements^{1,2}. Since Tucker's proposal³, many approaches have been developed to replace the elements in complementary metal-oxide semiconductor (CMOS) circuits⁴⁻⁹. SETs were also investigated after they were directly embedded in CMOS circuits⁸⁻¹⁰. Currently, conventional Si transistors are much smaller than SETs. SETs have attracted attention as charge sensors¹¹⁻¹³, which have been used for the readouts of silicon qubits¹⁴⁻¹⁶, or as current standards¹⁷⁻¹⁹.

The SET consists of a small metallic island or a d-generated semiconductor island surrounded by a source and drain via tunneling junctions with low capacitances. The SET yields periodic outputs referred to as Coulomb oscillations, which vary as a function of the gate voltage, and the oscillation period corresponds to the change in the number of electrons in the island. The maximum signal change in an SET is the difference between the peak and the trough of the Coulomb oscillation. The SET current is sensitive to electric potential variations on the SET island¹¹. The standard readout process of a spin qubit (spin in localized states, such as a single impurity or quantum dot (QD)) is a spin-to-charge conversion, and the change in charge of the localized state is detected by the SET current^{14,15,20,21}.

There are many methods for the detection of charges, such as the use of radiofrequency SETs (rf-SETs)^{15,20,21} and the direct measurement of the SET by a single GaAs amplifier^{22,23}. Inokawa *et al* showed that a Coulomb oscillation is effectively outputted by directly connecting the SET to an MOS field-effect transistor. They experimentally demonstrated multiple-valued logic by SETs operating at 27 K. The effectiveness of the series coupling of the SET with MOS transistors was also experimentally investigated by Uchida *et al.*¹⁰. Scalable SET sensing systems require scalable circuits. However, previous SET sensors¹⁴⁻¹⁹ did not explicitly consider the array of SETs as part of CMOS circuits.

In this study, we theoretically consider a scalable detection circuit based on the implementation of many SETs in CMOS circuits. Our basic concept of the amplification of

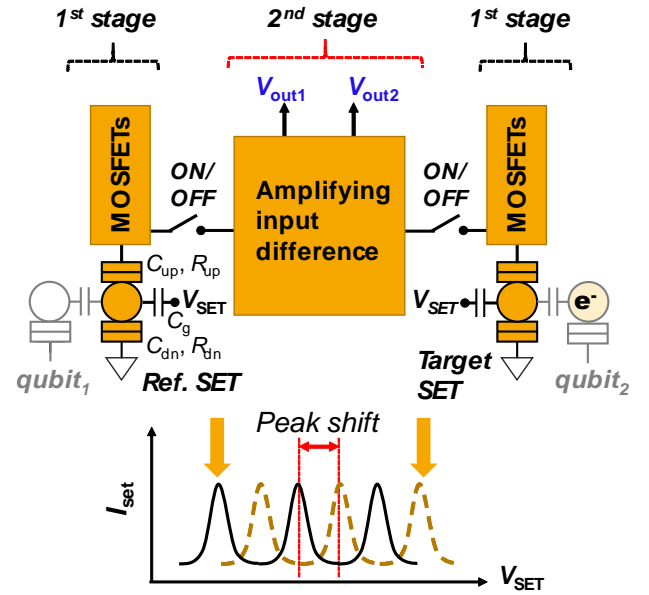


FIG. 1: Concept of our two-stage amplification circuit of the charge-sensing single-electron-transistor (SET). Instead of amplifying one SET sensor, we consider amplifying pairs of SETs that have different states with each other. Depending on the existence of the extra electron in the quantum dot (QD) outside the SETs, the electric potential of the island of the SETs changes. Throughout this paper, we model the effects of the electric potential of the QDs and V_{SET} by the gate voltages V_{G1} and V_{G2} of the SETs. The switches between the 1st and 2nd stages are typically realized by wordline nMOS transistors, using which we can select pairs of SETs among the SET array.

the SET signals consists of two stages, as shown in Fig. 1. The first amplification stage of the process is conducted by direct connection of the SET to pMOS transistors. In the second stage, we introduce a reference and a target SET and amplify the difference between two SETs using standard amplifier circuits, such as the differential amplifier (DA) circuits, and the static random-access memory (SRAM) cells.

For smooth connection to the digital circuits, the out-

put of the sensing circuit should be a digital signal (either a "0" or a "1"). For this purpose, it is better to compare the relative output of the target SET with that of the reference SET. In our application of the SRAM cell, the relative voltage difference between the target SET and the reference SET is found to be quickly latched to "0" or "1." This is in contrast to the measurements in Refs.^{14–16}, wherein the results were obtained after the analysis of a series of time-dependent SET currents. Our CMOS circuits are assumed to be close to the SETs. In addition, the target and the reference SETs are chosen by switching on the wordline transistors between the pairs of SETs and amplifiers. Then, the circuit using the pairs of SETs becomes more compact than the amplifying circuit of a single SET. Accordingly, our proposal is suitable for an array of sensing SETs.

In this study, we implement the current characteristics of the orthodox theory of the SET²⁴ into the SPICE (Simulation Program with Integrated Circuit Emphasis) circuit simulator based on the BSIM4 (Berkeley Short-channel transistor Model, level=54) by using the standard modeling language of the Verilog-A. We considered two types of SETs one of which is operated at low (4.2 K), and the other is operated at high temperatures (-30°C). At low temperatures, such as 4.2 K, the threshold voltage of the MOS transistors becomes higher because of the incomplete ionizations. Many studies regarding cryo-CMOS^{25–28} have been conducted to determine the model parameters at low temperatures. However, the general compact model is not available for such low temperature. In addition, the basic CMOS operations are basically the same as that at room temperature (RT). Thus, we applied the CMOS parameters that are available in the conventional SPICE models to the CMOS parts for both types of the SETs. In the following, circuit calculations are mainly conducted at $T = -30^\circ\text{C}$, which is in the range of the conventional models.

We consider CMOSs with gate lengths of $L = 90$ nm and $L = 65$ nm, whose drain voltages V_D are 1.2 V and 1.0 V, respectively. We also consider the effects of small variations in the SETs and CMOS transistors. The purpose of the comparison of pairs of SETs is to detect the changes in the Coulomb oscillations of the target SET. Thus, given that the voltage difference between the peak and trough currents of the Coulomb oscillations can be distinguished, we will be able to detect the changes of the target SET even if there are variations in the devices.

Herein, we consider four SETs, as listed in Table I. The LT-SET t (target) and LT-SET r (reference) are operated at 4.2 K, and RT-SET t and RT-SET r can operate at -30°C. The parameters of the LT-SET t (RT-SET t) exhibit 10% variations compared with those of the LT-SET r (RT-SET r). The calculated current–voltage characteristics (I_D - V_D) are listed in the appendix. The charging energy is given by $E_c \equiv e^2/[2(C_{\text{up}} + C_{\text{dn}} + C_g)]$. The magnitude between the peak and trough currents is on the order of pA, and its voltage change estimated by $\text{pA} \times 25.9 \text{ k}\Omega = 25.9 \text{ }\mu\text{V}$ is very small (25.9 k Ω is a quantum resistance¹). On the other hand, the variations in the

TABLE I: The four SETs we use here.

SET	Capacitance(aF)			Resistance(Ω)		Temp(K)	E_c (meV)
	C_{up}	C_{dn}	C_g	R_{up}	R_{dn}	T	
LT-SET r	1	10	2	100k	1M	4.2	6.16
LT-SET t	1.1	0.9	2.2	110k	0.9M	4.2	6.51
RT-SET r	0.1	0.5	0.5	100k	500k	243	72.8
RT-SET t	0.11	0.45	0.45	110k	450k	243	79.3

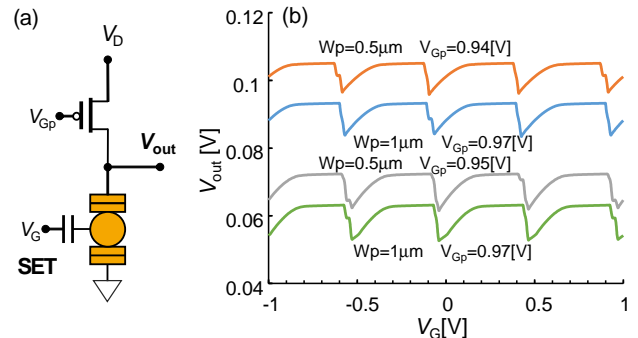


FIG. 2: First-stage amplification circuits, where the LT-SET t (see table I) and pMOS are directly connected. The output voltage V_{out} is amplified depending on the gate voltage V_{Gp} of the pMOS. Depending on the width of the pMOS ($W_p = 0.5 \text{ }\mu\text{m}$ and $W_p = 1 \text{ }\mu\text{m}$), the optimal points change. The Coulomb oscillation is amplified up to approximately 10 mV ($V_D = 1.2 \text{ V}$). Hereafter we use $W_p = 0.5 \text{ }\mu\text{m}$ pMOS at the 1st stage.

threshold voltage V_{th} of conventional CMOSs are generally on the order of millivolts. Therefore, we need to amplify the SET outputs before connecting the SETs to conventional CMOS circuits.

We start from the first amplification stage in which the SET is directly connected to the CMOS transistors, as shown in Fig. 2(a). By a series connection, the low SET current value increases with CMOS⁸. Figure 2(b) shows that the amplification of the SET signal becomes prominent at $V_{Gp} \gtrsim 0.9 \text{ V}$. The distortions of the waveforms compared with the original Coulomb oscillations originate from the nonlinearity of the I_D - V_D characteristics of the pMOS transistors. We analyze the amplification mechanism based on the standard long-channel model²⁹. The I_D - V_D of CMOS transistors depends on the triode region $|V_{DS}| < |V_{GS} - V_{th}|$ and the saturation region $|V_{DS}| > |V_{GS} - V_{th}|$. At present, amplification is observed in $|V_{DS}| = |V_{\text{out}} - V_D| \approx 1.05 \text{ V} > |V_{GS}| = |V_{Gp} - V_D| = 0.15 \text{ V}$ (saturation region). We did not observe a sufficiently large amplification in the triode region. The SET current I_{SET} under large source-drain voltage is approximately described by $I_{\text{SET}} \propto V_{\text{SET}}$ (see appendix). More explicitly we assume that $I_{\text{SET}} \approx V_{\text{SET}}/R_D$. Thus, we can write the I_D - V_D characteristics in the saturation re-

gion; further, the SET given by

$$I_D = \frac{1}{2}\beta_p(V_{Gp} - V_D - V_{thp})^2(1 + \lambda(V_D - V_{out})), (1)$$

$$V_{out} \approx R_D I_D. (2)$$

The solution of these equations is given by

$$V_{out} = \frac{1 + \lambda V_D}{1 + \lambda I_{D0} R_D} I_{D0} R_D, (3)$$

where $I_{D0} \equiv \frac{1}{2}\beta_p(V_{Gp} - V_D - V_{thp})^2$. Because $I_{D0} R_D < V_D$, the SET output is enhanced by $\frac{1 + \lambda V_D}{1 + \lambda I_{D0} R_D} > 1$. Note that λ is conspicuous in both the $L = 90$ nm and $L = 65$ nm pMOS transistors (see appendix), and we can see that the output voltage oscillates around ~ 10 mV in Fig. 2(b).

The second-stage amplification is conducted using standard amplifier circuits. Figure 3 shows the results obtained from a basic DA circuit. Note that the gate voltages V_{G1} and V_{G2} represent the shifted electrical potential V_{SET} by the additional sensing QD in Fig. 1. Conventional DAs amplify two inputs with opposite phases. In the case of SETs, two different phases of Coulomb oscillations are input. We consider that the two SET signals possessing different current peaks mimic the two input signals of the conventional DA with different phases. In Figs. 3(b), we show the results for the output voltage difference of $V_{out2} - V_{out1}$ for a fixed $V_{G1} = 0$. The voltage difference $V_{out2} - V_{out1}$ increases by approximately 40 mV for $L = 90$ nm (the results for $L = 65$ nm are shown in the appendix), and can be detected by conventional CMOS amplifier circuits (the following circuits after V_{out2} and V_{out1} are not shown). This enhancement of the Coulomb oscillations is the result of the two-stage amplification of SET signals.

The magnitude of the enhancement of the Coulomb oscillation in Fig 3(b) changes depending on the threshold voltage variations of the eight MOS transistors. In Fig.3(c), we provide the distribution of the difference in the peak and trough of $V_{out2} - V_{out1}$ obtained through over 300 Monte Carlo simulations of the threshold variations with LT-SET t and LT-SET r at $V_{G1} = 0$ and $V_{G2} = 0.2$ V. The number of small amplitudes of $|V_{out2} - V_{out1}|$ (< 5 meV) is nine out of 300 samples. Small amplitudes of $V_{out2} - V_{out1}$ can be avoided by applying different voltages such as V_{Gpi} and WL_i on each part of the DA.

We now consider the application of the standard SRAM cell containing six MOS transistors³⁰ to detect a pair of SETs, as shown in Fig. 4(a). Figure 4(b) shows the simulation results of the time-dependent SRAM cell outputs V_{out1} and V_{out2} of the two LT-SETs. We can see that $V_{out1} < V_{out2}$ for $V_{G2} = 0.1$ V, but $V_{out1} > V_{out2}$ for $0.15 \text{ V} \leq V_{G2} \leq 0.4 \text{ V}$ for $L = 90$ nm devices. This implies that the shift in the electric potential of the sensing QD from $V_{G2} = 0.1$ V to $V_{G2} = 0.15$ V changes the electric potential of the target SET island, resulting in a change in the relative magnitude between V_{out1} and V_{out2} . Figure 4(c) replots $V_{out2} - V_{out1}$ in Fig. 4(b) as a function of V_{G2} with the results for $L = 65$ nm at time 10^{-8} s. Thus, we can detect the change in the target SET represented by V_{G2} by measuring the relative outputs of the

SRAM cell. Herein, the initial voltage at the SRAM cell input is set to $V_D/2$, and stray capacitances of 0.2 pF are included at the input nodes of the SRAM cell (Figures not shown). As the stray capacitance increases, the time to split increases.

In general, SRAM cells undergo initial threshold voltage V_{th} variations³¹, and we have to consider these variations in the MOS transistors as well as the two SETs. Here, we extend the SRAM cell circuit to a dynamic random-access memory (DRAM)-like structure^{32,33} in Fig. 5(a), where it is considered that the equalizer circuit mitigates the voltage difference of the wordlines between the two SETs. Figures 5(b)(c) show two types of readouts for the two types of SETs. The equalizer voltage is switched on at 1 ns and stopped after 2 ns. The SAN and SAP voltages are switched on after the equalizer at $t = 6$ ns and $t = 8.5$ ns. The wordlines are switched on at 4 ns. We can see that the change in the gate voltage V_{G2} , which corresponds to the existence of the charge sensor QD, causes the outputs V_{out1} and V_{out2} to change from $V_{out1} > V_{out2}$ to $V_{out1} < V_{out2}$.

In a realistic situation, it is possible that the temperature changes. Therefore, we also calculated the temperature dependence of the amplifier response. It is desirable that the relative magnitude of V_{out1} to V_{out2} does not change even when the operating temperature changes. The temperature dependencies of the characteristics of the DA (Fig. 3) and DRAM (Fig. 5) are robust against temperature changes as long as the temperature change is sufficiently small on the order of several tens of degrees (see appendix).

Considering that there are variations in SETs and MOS transistors, we may have to check and record the basic characteristics of each device at the first calibration stage of the chip. The I - V characteristics of each SET should be clarified before using the charge-sensing SET. This information is stored in the extra SRAM or other memories, and becomes the overhead of the system. An effective method for determining the optimal biases automatically is a future issue. It is possible that the applied voltages destroy the SET charge states. However, herein, we neglected the effects of the backaction from the CMOS circuits. Hence, the assessment of the backaction remains a future issue.

In conclusion, we proposed two-stage amplification circuits for SETs. Based on serial connections with MOS transistors and a comparison with the reference SET, we numerically show that the readout of the charge-sensing SET is greatly enhanced. We also considered the effects of variations in the MOS transistors and SETs, and show that as long as the variations are small, the two SETs can be compared effectively.

DATA AVAILABILITY

The data that supports the findings of this study are available within the article.

Acknowledgments

We are grateful to T. Mori and H. Fuketa for the fruitful discussions. We are also grateful to Y. Yamamoto for his technical support in using SmartSpice. This work was partly supported by MEXT Quantum Leap Flagship Program (MEXT Q-LEAP) Grant Number JP-MXS0118069228, Japan.

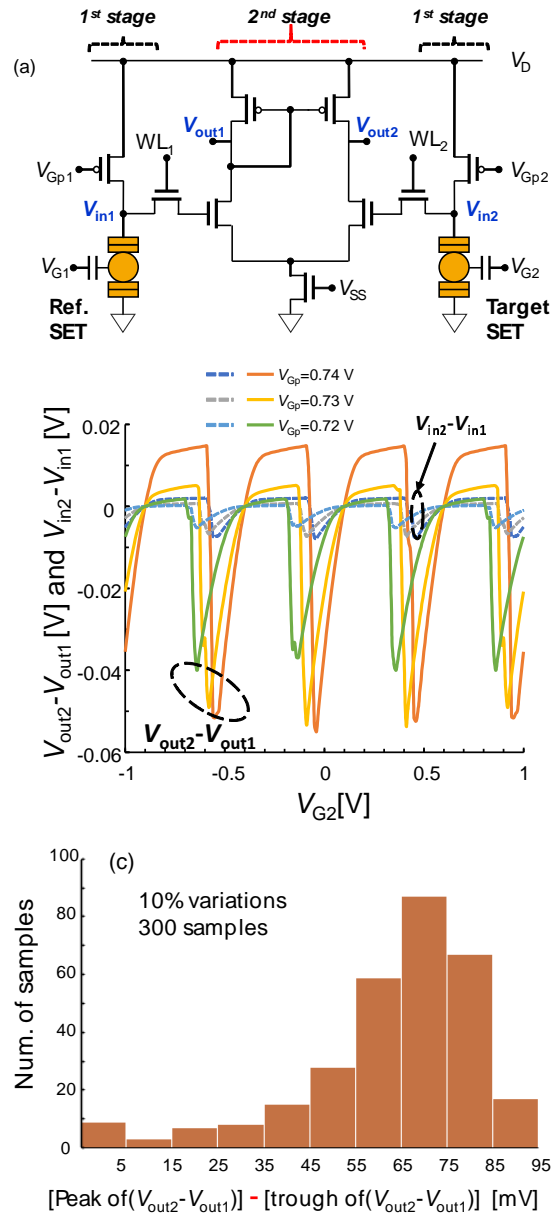


FIG. 3: (a) The differential amplifier (DA) is applied at the 2nd stage amplification of Fig.1. (b) Numerical results of $V_{out1} - V_{out2}$ (enhanced Coulomb oscillations) for $L = 90$ nm at $V_{G1} = 0$. $V_{Gp1} = V_{Gp2} = V_{Gp}$. The pMOS and nMOS widths of the DA are given by $W_{pa} = 1 \mu\text{m}$, and $W_{na} = 10 \mu\text{m}$, respectively. The widths of the wordline nMOS and 1st stage pMOS are given by $W_n = 5 \mu\text{m}$ and $W_p = 0.5 \mu\text{m}$, respectively. $V_D = 1.2$ V. We can see that the amplitude of $V_{out2} - V_{out1}$ is approximately 40 mV, which is larger than the amplitude of the input $V_{in2} - V_{in1}$. (c) Histogram of the Monte Carlo simulation of the output difference when the V_{th} of all CMOS transistors varies by 10% over 300 simulations.

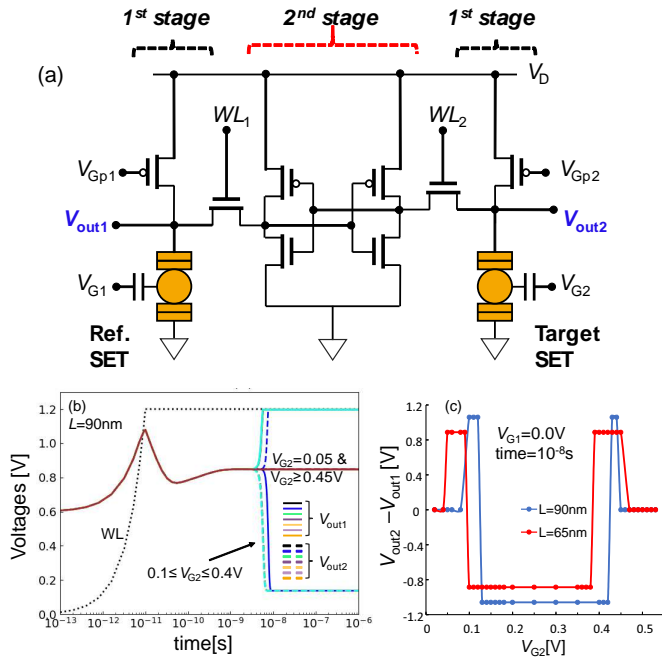


FIG. 4: (a) Six transistor static random-access memory (SRAM) cell applied in the 2nd-stage amplification of Fig. 1. (b) Time dependent voltage behaviors of the SRAM setup of $L=90$ nm for widths $W_n = 0.5 \mu\text{m}$ and $W_p = 1.2W_n$. The width of the WL transistor is $0.4 \mu\text{m}$. $V_{Gp} = 0.55$ V and $V_{G1} = 0.0$ V using the LT-SETs. The change in V_{out1} and V_{out2} is in the range of $V_{G2} = \{0, 0.05, 0.1, 0.15, 0.2, 0.25, 0.3, 0.35, 0.4, 0.45, 0.5\}$ V. (c) Replotting of (b) as a function of V_{G2} of (b) and the result for $L = 65$ nm.

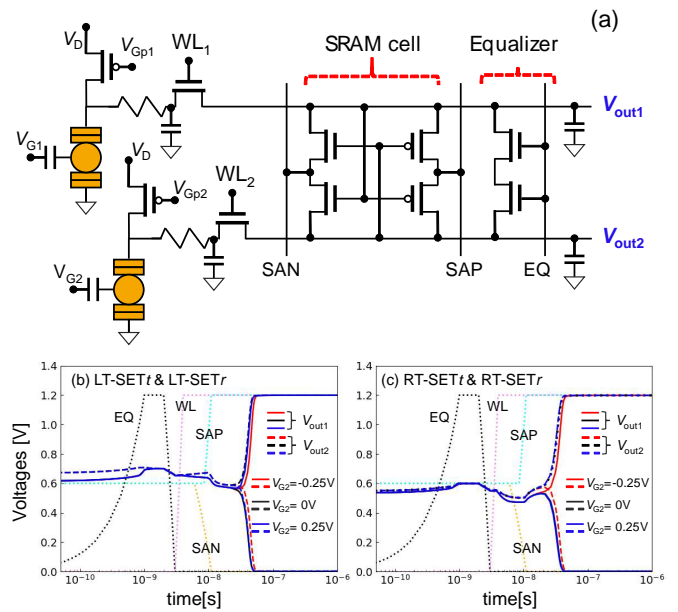


FIG. 5: (a) Dynamic RAM (DRAM)-like detection circuits are applied at the 2nd stage amplification of Fig. 1. The stray capacitance of 1 pF is added to the nodes V_{out1} , V_{out2} , inputs of the SETs, and equalizer circuits. (b)(c) Time-dependent characteristics of the different SET pairs (the LT-SET pair in (b) and RT-SET pair in (c)) in Fig. (a) with 10% threshold voltage variations in the MOS transistors. The pulse sequence is constituted following the standard DRAM sequence of Ref.^{32,33}. $V_{G1} = 0$ is fixed and V_{G2} changes. Depending on whether $V_{G1} > V_{G2}$ or $V_{G1} < V_{G2}$, the outputs V_{out1} and V_{out2} change from $V_{out1} > V_{out2}$ to $V_{out1} < V_{out2}$. The widths of the nMOS and pMOS are $0.5 \mu\text{m}$ and $0.6 \mu\text{m}$. The width of the equalizer nMOS is $20 \mu\text{m}$. The width of the WL transistor is $0.6 \mu\text{m}$. ($V_{Gp1} = V_{Gp2} = 0.87$ V, $L = 90$ nm).

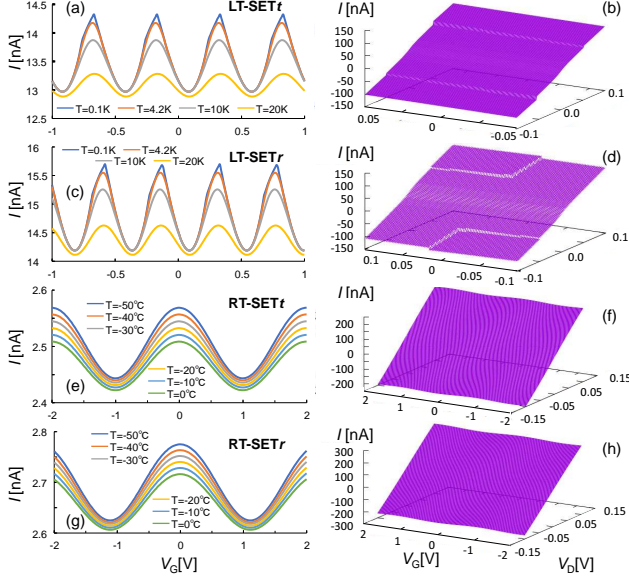


FIG. 6: Current-voltage characteristics of SETs calculated based on the orthodox theory. (a)(c)(e)(g) Temperature dependence of the $I_{\text{SET}} - V_G$ characteristics at $V_D = 0.01$ V. (b)(d) Three-dimensional (3D) view of I_{SET} for $T = 0.1$ K. (f)(g) 3D view of I_{SET} for $T = -30^\circ\text{C}$. (a)(b) $C_{\text{up}} = 1$ aF, $C_{\text{dn}} = 10$ aF, $C_g = 2$ aF, $R_{\text{up}} = 100$ k Ω , $R_{\text{dn}} = 1$ M Ω (LT-SETt in Table I). (c)(d) $C_{\text{up}} = 1.1$ aF, $C_{\text{dn}} = 9$ aF, $C_g = 2.2$ aF, $R_{\text{up}} = 110$ k Ω , $R_{\text{dn}} = 0.9$ M Ω . (LT-SETr in Table I). As the asymmetry of the two junctions becomes larger, the Coulomb staircase becomes clearer. (e)(f) $C_{\text{up}} = 0.1$ aF, $C_{\text{dn}} = 0.5$ aF, $C_g = 0.5$ aF, $R_{\text{up}} = 100$ k Ω , $R_{\text{dn}} = 500$ k Ω (RT-SETt in Table I). (g)(h) $C_{\text{up}} = 0.11$ aF, $C_{\text{dn}} = 0.45$ aF, $C_g = 0.45$ aF, $R_{\text{up}} = 90$ k Ω , $R_{\text{dn}} = 450$ k Ω (RT-SETr in Table I).

Appendix A: SET characteristics determined by the orthodox theory

Figure 6 shows the current-gate voltage characteristics of the four SETs used in the main text, calculated based on the orthodox theory²⁴. The Coulomb staircase becomes clearer for a large asymmetry between the two tunnel junctions; however, the amplitude of the oscillation becomes smaller. Therefore, we consider the case of a smaller asymmetry. The wide-range view of the current-voltage ($I_D - V_D$) characteristics of the SET shown in Figs. 6(b)(d)(f)(h) enables the approximation of $V_D \propto I_D$ of Eq.(2) in the main text.

Appendix B: Additional results for the transistors and amplification circuits

Figure 7 shows the basic $I_D - V_D$ characteristics of the pMOS transistors used herein (Berkeley short-channel transistor model BSIM-4), and Fig. 8 shows the characteristics of the DA circuits of Fig. 3 (b) for $L = 65$ nm. Although amplification is not observed in the triode region, herein, we show that amplification can be expected

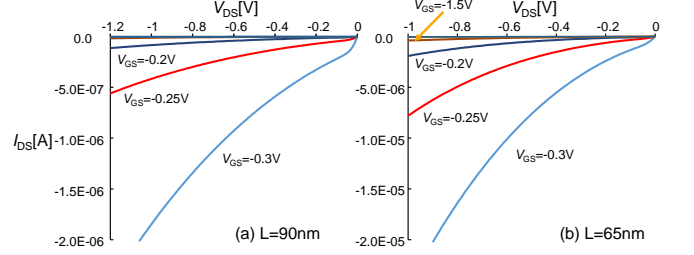


FIG. 7: $I_D - V_D$ characteristics of the pMOS transistors at -30°C . (a) $L = 90$ nm and (b) $L = 65$ nm.

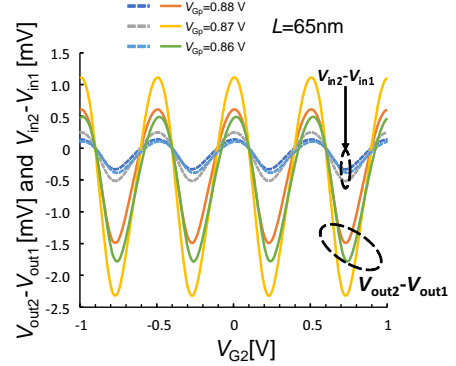


FIG. 8: Numerical results of the two outputs $V_{\text{out}1}$ and $V_{\text{out}2}$ of the differential amplifier circuit for $L = 65$ nm for a fixed $V_{G2} = 0$. The transistor sizes are the same as those in Fig. 3 in the main text.

even in the triode region. In the triode region, Eq. (1) is replaced by

$$I_D = \beta_p (V_{Gp} - V_D - V_{\text{thp}} - [V_D - V_{\text{out}}]) [V_D - V_{\text{out}}] \quad (\text{B1})$$

where $\beta_p \equiv \mu_p C_{\text{ox}} \frac{W}{L}$ and $\lambda (< 1)$ are the channel length modulation coefficients (L , W , C_{ox} , and μ_p are the length, width, gate capacitance and mobility of the pMOS, respectively). The solution to the equations is given by

$$V_{\text{out}} \approx V_D + 2v_{\text{gp}} - \frac{1}{R_D \beta_p}, \quad (\text{B2})$$

where $v_{\text{gp}} = V_{Gp} - V_D - V_{\text{thp}}$. Eq. (B2) shows that the SET output changes the rate of $R_D \partial V_{\text{out}} / \partial R_D \approx 1 / [\beta_p R_D]$. When we take $\mu_p = 0.025$ m²/(Vs), $C_{\text{ox}} = \epsilon_0 \epsilon / t_{\text{ox}}$ with $\epsilon = 3.9$ and $t_{\text{ox}} = 4$ nm for $L = 90$ nm and $W_p = 0.5$ μm , we have $\beta_p = 0.0002397$ AV⁻² and $\beta_p R_D = 2.397 \times 10^2$ V⁻¹ for $R_D = 1$ M Ω . Then the change rate $R_D \partial V_{\text{out}} / \partial R_D \approx 4.17$ mV. Whether the triode region or the saturation region is better for the amplification depends on the current characteristics of the MOS transistors.

Appendix C: Temperature dependence

We calculated the temperature dependence of the amplifier response. It is desirable that the relative magni-

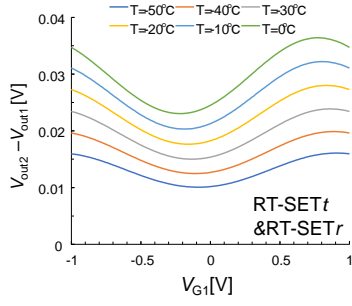


FIG. 9: Temperature dependence of $V_{out1} - V_{out2}$ in Fig. 3(a) of $L=90$ nm MOS transistors for different SETs as a function of V_{G1} . $V_{G2}=0.1$ V. The left SET is the RT-SET $_t$ and the right SET is the RT-SET $_r$.

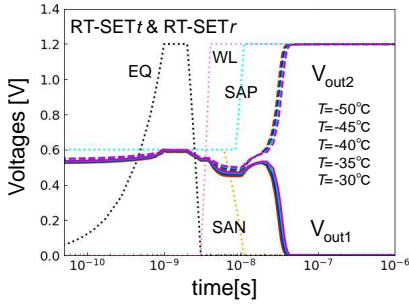


FIG. 10: Temperature-dependent characteristics for $V_{G2} = 0.2$ V ($L=90$ nm). The widths of the nMOS and pMOS in the circuits are $0.5 \mu\text{m}$ and $0.6 \mu\text{m}$. The width of the equalizer nMOS is $20 \mu\text{m}$. $V_{Gp1} = V_{Gp2} = 0.87$ V.

tude of V_{out1} to V_{out2} does not change as long as the operating temperature changes in the range of approximately $-50^\circ \sim 0^\circ\text{C}$. Figures 9 and 10 show the temperature dependence of the characteristics of the DA (Fig. 3), and DRAM (Fig. 5). For example, depending on the value of V_{Gp} , we can observe the relative change in the magnitude between V_{out1} and V_{out2} . We also observe that even when there are variations, the two SETs can be differentiated by changing the gate voltage V_{G1} or V_{G2} . The strength to the change of temperature depends on each operation region.

Appendix D: Detection by cross-coupled circuit

Figure 11(a) shows our other proposal based on the cross-coupled type. In this case, two SETs are series-

connected to cross-coupled MOS transistors, where the changes in the SET signals are directly transferred to the MOS transistors. Herein, the 10% variations between the SETs and among the MOS transistors are considered. To observe the change in V_{G2} to the fixed V_{G1} , we have to adjust the wordline voltages. In Figs. 11(b) and 11(c), the wordline voltage of the left SET is reduced to $WL_1 \approx 0.84$ V, and $WL_1 \approx 1.08$ V, respectively. In Fig. 11(b)(c), V_{out2} becomes higher than V_{out1} between

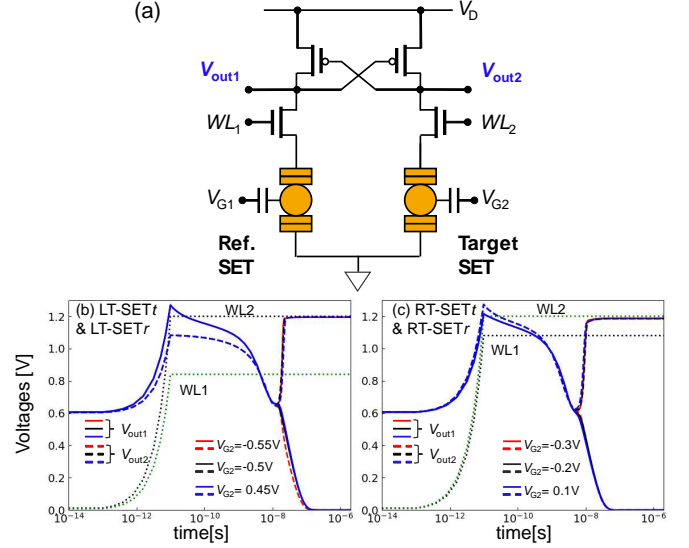


FIG. 11: (a) Cross-coupled type readout of two pairs of SETs. (b)(c) Time-dependent output characteristics of the cross-coupled type assuming 10 % variations in the threshold voltage of the MOS transistors (the LT-SET pair in (b) and RT-SET pair in (c)). The two wordline voltages are adjusted to change the relation between V_{G1} and V_{G2} when V_{G2} changes. The wordline voltages are switched on at 10 ps with a rising time of 10 ps. $W_n = 5 \mu\text{m}$, $W_p = 0.1 \mu\text{m}$ and $V_{G1}=0$ V.

$V_{G2} = -0.55$ V and $V_{G2} = -0.5$ V ($V_{G2} = -0.3$ V and $V_{G2} = -0.2$ V). When there are no variations, the left and right hand circuits are exactly the same, and V_{out1} and V_{out2} are clearly split depending on the gate voltages of the two SETs. Temperature changes are not observed, similar to the case with the SRAMs mentioned above (Figures not shown).

* Electronic address: tanamoto@ics.teikyo-u.ac.jp

¹ H. Grabert and M. H. Devoret, "Single Charge Tunneling: Coulomb Blockade Phenomena In Nanostructures" (Nato Science Series B:)(Springer, New York, 1992).

² K. K. Likharev, Proc. IEEE, **87**, 606 (1999).

³ J. R. Tucker, J. Appl. Phys. **72**, 4399 (1992).

⁴ R. H. Chen, A. N. Korotkov, and K. K. Likharev, Appl. Phys. Lett. **68**, 1954 (1996).

⁵ S. Tiwari *et al.*, Appl. Phys. Lett. **68**, 1377 (1996).

⁶ K. Uchida *et al.*, Jpn. J. Appl. Phys. **38**, 4027 (1999).

⁷ S. Mahapatra and A. M. Ionescu, 4th IEEE Conference on Nanotechnology p.287 (2004).

- ⁸ H. Inokawa, A. Fujiwara and Y. Takahashi, IEEE Trans. Electron Devices, **50**, 462 (2003).
- ⁹ K. Yano *et al.*, 1999 IEEE International Electron Devices Meeting **87**, 633 (1999).
- ¹⁰ K. Uchida *et al.*, Digest of ISSCC 2002, 206 (2002).
- ¹¹ M. Field, C. G. Smith, M. Pepper, D. A. Ritchie, J. E. F. Frost, G. A. C. Jones, and D. G. Hasko, Phys. Rev. Lett. **70** 1311 (1993).
- ¹² D. Berman J. Vac. Sci & Tech. B **15**, 2844 (1997)
- ¹³ A. M. Ionescu, M. J. Declercq, S. Mahapatra, K. Banerjee and J. Gautier, Proceedings 2002 Design Automation Conference pp. 88-93 (2002).
- ¹⁴ A. Morello, *et al.*, Nature **467**, 687 (2010).
- ¹⁵ Gonzalez-Zalba *et al.*, Nat Commun **6**, 6084 (2015).
- ¹⁶ N. Shaji *et al.*, Nature Phys **4**, 540 (2008).
- ¹⁷ A. Fujiwara, *et al.*, Appl. Phys. Lett. **88**, 053121 (2006).
- ¹⁸ K. Nishiguchi and A. Fujiwara, 2007 IEEE International Electron Devices Meeting, 791 (2007).
- ¹⁹ S. P. Giblin *et al.*, Metrologia **57**, 025013 (2020).
- ²⁰ R. J. Schoelkopf *et al.*, Science **280**, 1238 (1998).
- ²¹ W. Lu, Z. Ji, L. Pfeiffer, K.W. West, and A.J. Rimberg, Nature **423**, 422 (2003).
- ²² J. Petersson *et al.*, Phys. Rev. B **53**, 13272 (1996).
- ²³ E. H. Visscher *et al.*, Appl. Phys. Lett. **68**, 2014 (1996).
- ²⁴ M. Amman, R. Wilkins, E. Ben-Jacob, P. D. Maker, and R. C. Jaklevic, Phys. Rev. B **43**, 1146 (1991).
- ²⁵ R. R. Green, Rev. Sci. Instrum., **39**, 1495 (1968).
- ²⁶ F. H. Gaensslen, V. L. Rideout, E. J. Walker and J. J. Walker, IEEE Trans. Electron Devices, **24**, 218 (1977).
- ²⁷ A. Beckers, F. Jazaeri, A. Ruffino, C. Bruschini, A. Baschirotto and C. Enz, 2017 47th European Solid-State Device Research Conference (ESSDERC), p. 62, (2017).
- ²⁸ J. van Dijk *et al.*, 2020 IEEE Custom Integrated Circuits Conference (CICC), p. 1, (2020).
- ²⁹ Y. Taur and T. H. Ning, "Fundamentals of Modern VLSI Devices" (Cambridge University Press, 1998).
- ³⁰ E. Seevinck, F. J. List and J. Lohstroh, IEEE J. Solid-State Circuits, **22**, 748 (1987).
- ³¹ D. E. Holcomb *et al.*, IEEE Trans. Comput. **58**, 1198 (2009).
- ³² B. Keeth and R. J. Baker, "DRAM Circuit Design: A Tutorial" (John Wiley & Sons, 2001).
- ³³ B. Jacob, D. Wang, and S. Ng, "Memory Systems: Cache, DRAM, Disk" (Morgan Kaufmann; 1st edition, Amsterdam 2007).